Journal of Applied Fluid Mechanics, Vol. 17, No. 1, pp. 251-260, 2024.
Available online at www.jafmonline.net, ISSN 1735-3572, EISSN 1735-3645.
https://doi.org/10.47176/jafm.17.1.1962

Numerical and Experimental Investigation of Flow Induced Vibration of an Ejector Considering Cavitation

Y. Zhang, C. He, P. Li† and H. Qiao

Nuclear Power Institute of China, Chengdu, 610213, China

†*Corresponding Author Email: pengzhouli@aliyun.com*

ABSTRACT

As one of the essential components of the conventional island in a nuclear power plant, the ejector supplies cooling water to the reactor core in an accident state. It needs serious maintenance for its structural stability. The flow-induced vibration of an ejector in service was numerically examined in this research while taking the cavitation phenomenon into account. To achieve this goal, a bidirectional fluid–structure interaction simulation based on the ANSYS platform was run. In our lab, an experimental loop was also set up to validate the fluid model. Then, under specific circumstances, it was possible to monitor the cavitation revolution process, pressure variation, and ejector vibration. According to the numerical results, the distribution of the vapor phase is largely found in the mixing and diverging portions, and it changes over time. In the ejector, a significant wideband excitation was observed. Additionally, the von Mises stress and flow-induced vibrational features of the ejector structure were investigated.

Article History

Received April 28, 2023
Revised September 2, 2023
Accepted September 13, 2023
Available online November 1, 2023

Keywords:

Numerical simulation
Flow induced vibration
Fluid-structure interaction
Ejector system
Cavitation

1. INTRODUCTION

Nuclear power has received considerable attention because of its advantages such as zero greenhouse gas emissions, clean properties, and superior generating efficiency. Interest in reactor components is growing globally (Santis et al., 2018; Park et al., 2019). Numerous systems have been designed to support reactor operation. An ejector system protects the reactor core from damage by distributing heat in the event of an accident or emergency shutdown. In this system, the ejector plays a crucial role in the supply of coolant, which is realized by the siphon effect (Haghparast et al., 2018). Ejectors have also been used in other applications, such as heat-pump systems, because of their low cost, simplicity, and ease of maintenance (Dai et al., 2023). Despite the importance of the ejector, faulty structural design or unforeseen circumstances can result in excessive vibration of the pipes connected to the ejector, which is a common vibration issue caused by flow in engineering (Ashish et al., 2016; Liu et al., 2019; Javadi et al., 2021). The hydraulic behavior of the ejector is more complex than that of typical components because it is subjected to a mixed flow that includes the operating and suction media. In addition, potential transient flow directly affects the dynamic properties of the ejector. According to Tang et al. (2019), cavitation is a potential event that is the primary cause of structural instability or even damage.

The violent vibrations of pipelines in ejector systems are mainly caused by cavitation, which occurs when the local pressure is below the saturated vapor pressure. During cavitation, many micron-sized bubbles are initially produced, which collapse with pressure recovery. The energy released during the cavitation process is the main source of pipeline vibration. Numerous studies have been conducted on structural responses to cavitation. For example, Asi (2006) conducted an investigation on the failure related to a diesel engine injector nozzle. By analyzing the failure zones via visual evaluation and chemical testing, they concluded that the failure was caused by cavitation near the internal surface of the structure. Sarkar et al. (2021) provided a one-way coupling method to simulate the interaction between the fluid and solid domains. Based on this method, the deformation mechanism of a solid subjected to cavitation was revealed. Moreover, the effects of different materials and distances between the bubbles and solid walls on the deformation were studied in detail. To avoid the coupling of traditional fluid and solid solvers, Joshi et al. (2019) developed a meshless particle method to investigate the collapse of cavitation bubbles and the erosion of structures. In their study, the fluid and structure responses were calculated in an

integrated solver, and a non-dimensional parameter, the effective pressure, was rendered, which predicted the plastic strain location well. In general, vibration in the pipeline of an ejector system is a typical flow-induced vibration (FIV) behavior. FIV is categorized as a fluid–structure interaction (FSI) issue, which refers to the phenomenon in which structures are immersed in a fluid or conveying fluid vibration owing to the interaction of the fluid, damping, and elastic forces, which comprise complex mechanisms (Li et al., 2021; Zhang et al., 2022). Some studies have focused on the ejector system flow field and pressure fluctuation. For example, Banasiak et al. (2012) systematically evaluated the internal fluid field using numerical and experimental approaches. Several geometric ejector structures with various mixing lengths, diameters, and divergence angles were designed to determine the optimal configuration. Besagni and Inzoli (2017) presented a numerical study of a supersonic ejector pertaining to the internal static pressure distribution. Simulations with different turbulence models and geometries were conducted to identify applicable scenes. They pointed out that the SST k-ω model predicts better performance in terms of global and local flow phenomena. Ruangtrakoon et al. (2013) employed a numerical technique to study the influence of the nozzle shape on the ejector performance in a jet refrigeration cycle. Although many studies have focused on the cavitation phenomenon, there is a lack of a quantitative understanding of how cavitation affects fluid pressure fluctuations and the structural response of the ejector. Obtaining insight into the relationship between cavitation and the ejector response is beneficial for determining vulnerable structural areas and raising the safety margin.

In the present study, a bidirectional FSI simulation was conducted to characterize cavitation, pressure fluctuation, and structural vibration. The transient flow field evolution and vibration behaviors (deformation and stress) were observed. In addition, the frequency-domain characteristics of the fluid pressure and structural motion were studied using fast Fourier transform (FFT).

2. FLUID–STRUCTURE INTERACTION (FSI) SIMULATION FRAME

2.1 Simulation Process of Fluid–Structure Interaction

In this study, we considered both the pipe vibration of the ejector system excited by the fluid force and the flow field disturbance caused by structural deflection. Therefore, a bidirectional FSI simulation was performed using the multifield coupling analysis module of ANSYS. Two solvers exchange data: one is a computational fluid dynamics (CFD) solver based on the finite volume method and the other is a structural response solver using the finite element (FE) method in each calculation substep. The simulation data comprising the flow pressure and structural deformation were converted through the fluid–structure interfaces. The two solvers were connected using a system-coupling module. To guarantee the continuity of the displacement and traction on the interfaces, the following equations should

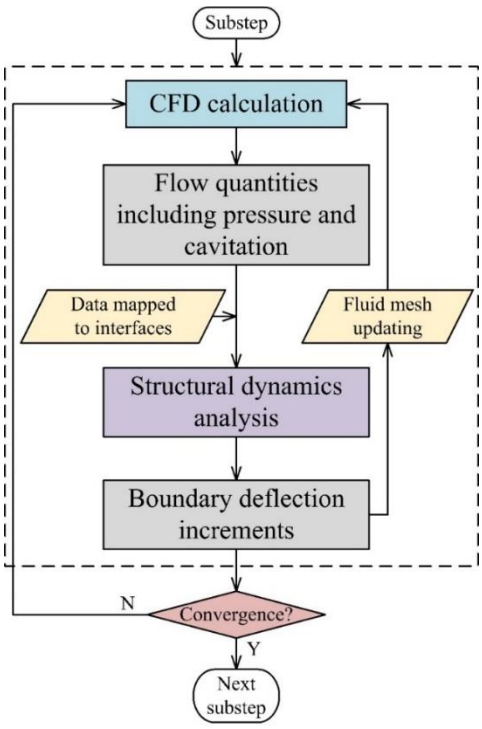

Fig. 1 Flow diagram of FSI simulation

be satisfied during the simulation process (Xie et al., 2020):

$$\boldsymbol{d}_{\mathrm{f}} = \boldsymbol{d}_{\mathrm{s}} \tag{1}$$

$$\boldsymbol{n} \cdot \boldsymbol{\sigma}_{\mathrm{f}} = \boldsymbol{n} \cdot \boldsymbol{\sigma}_{\mathrm{s}} \tag{2}$$

where $\boldsymbol{d}_{\mathrm{f}}$ and $\boldsymbol{d}_{\mathrm{s}}$ denote the wall boundary deformations in the fluid and solid domains, respectively; $\boldsymbol{\sigma}_{\mathrm{f}}$ and $\boldsymbol{\sigma}_{\mathrm{s}}$ are the stress tensors in the fluid and solid domains, respectively; and $\boldsymbol{n}$ is the unit normal vector.

A brief overview of the bidirectional FSI process is as follows: As shown in Fig. 1, in an iterative substep, the fluid field is first solved via CFD analysis, and the pressure exerted on the structural surfaces is then mapped to the interfaces of the structure model. The structural responses, including deformation and stress, are calculated using a structural dynamics analysis under a fluid load. Subsequently, the boundary deflection increments are transformed into a CFD model for mesh updating. Smoothing and remeshing methods are introduced to solve the problem of fluid mesh regeneration. Specifically, a diffusion smoothing approach based on the boundary distance is designated, where the diffusion constant factor is 1.5. In the remeshing scheme, the maximum and minimum length scales are estimated according to the mesh sizes in the fluid domain. In this study, the convergence criterion of the FSI simulation was set to 0.01, considering the possible complex flow.

2.2 Formation of Ejector System

The main parts of the ejector system under consideration include the nozzle, suction segment, mixing section, and divergent section. An assembly

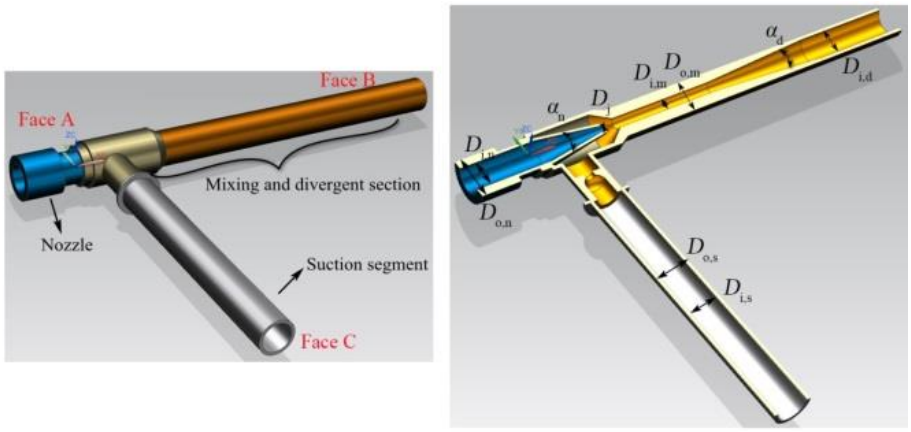

Fig. 2 Ejector system and some key size symbols

Table 1 Key sizes of ejector system

Symbol	Description	Value
$D_{o,n}$	Outer diameter of nozzle, mm	96.0
$D_{i,n}$	Inner diameter of nozzle, mm	66.9
$D_{o,s}$	Outer diameter of suction segment, mm	73.0
$D_{i,s}$	Inner diameter of suction segment, mm	66.9
$D_{o,m}$	Outer diameter of mixing section, mm	85.2
$D_{i,m}$	Inner diameter of mixing section, mm	31.5
$D_{i,d}$	Inner diameter of divergent section, mm	70.3
D_j	Diameter of jet, mm	16.1
α_n	Angle of nozzle, °	20.0
α_d	Angle of divergent section, °	8.0

drawing and appearance of these components are shown in Fig. 2(a). Some key size symbols are labeled in Fig. 2(b) within the 3D pattern. The values of these dimensions and their corresponding meanings are listed in Table 1.

2.3 CFD Model

The fluid media were identified as liquid water and vapor at a temperature of 313 K. In this model, both liquid water and vapor were treated as incompressible, adiabatic, and nonreactive. Because the main fountainhead triggers the vibration of pipelines, cavitation is of sufficient importance. A time step of 0.001 s was adopted to balance the efficiency and accuracy of the simulations. The entrances and outlets had specific pressures according to the actual situation. A moderate turbulence intensity of 4% was assumed at the flow boundaries, except at the walls.

A mixture model was applied to address the liquid–vapor two-phase flow. In this context, the continuity equation of the fluid can be formulated as

$$\frac{\partial \rho_m}{\partial t}+\nabla\cdot\left(\rho_m \boldsymbol{u}_m\right)=0 \tag{3}$$

where $\boldsymbol{u}_m$ denotes the mass-averaged velocity vector:

$$\boldsymbol{u}_m=\frac{\alpha_l\rho_l\boldsymbol{u}_l+\alpha_v\rho_v\boldsymbol{u}_v}{\rho_m} \tag{4}$$

ρ_m designates the mixture density:

$$\rho_m=\alpha_l\rho_l+\alpha_v\rho_v \tag{5}$$

where α is the volume fraction of each phase, ρ is the density of each phase, and subscripts l and v represent the liquid and vapor phases, respectively. At all entrances and outlets, the volume fraction of the vapor phase was set to zero, and the values in the interior fluid cell were automatically calculated.

The SST k-ω turbulence model together with the production limiter was adopted to approximate the elusive and chaotic turbulence flow in the ejector (Santis et al., 2018). The governing equations pertaining to k and ω can be expressed as follows:

$$\frac{\partial\left(\rho_m k\right)}{\partial t}+\frac{\partial\left(\rho_m k u_{m,i}\right)}{\partial x_i}=\frac{\partial}{\partial x_j}\left(\Gamma_k\frac{\partial k}{\partial x_j}\right)+G_k-Y_k+S_k \tag{6}$$

$$\frac{\partial\left(\rho_m \omega\right)}{\partial t}+\frac{\partial\left(\rho_m \omega u_{m,i}\right)}{\partial x_i}=\frac{\partial}{\partial x_j}\left(\Gamma_\omega\frac{\partial \omega}{\partial x_j}\right)+G_\omega-Y_\omega+S_\omega \tag{7}$$

where G refers to the generation of k or ω, Y the dissipation of k or ω due to turbulence, and S the user-defined source terms (zero here). Γ is the effective diffusivity, which is given by

$$\Gamma_{k,\omega} = \mu + \frac{\mu_t}{\sigma_{k,\omega}} \tag{8}$$

where $\sigma_{k,\omega}$ is the turbulence Prandtl number for k or ω, and μ_t is the turbulent viscosity. More detailed information about SST k-ω turbulence model can be found in Menter (1994).

To satisfy the requirements of the turbulence model for the boundary layer, 15 layers of inflation grids were formed in the vicinity of the inner walls of the ejector with an expansion ratio of 1.2. This study employed the SIMPLE algorithm to couple the velocity and pressure terms, and a second-order upwind scheme was used to discretize the momentum and turbulence terms in the spatial dimension for higher precision. Moreover, the PRESTO! and QUICK schemes were applied to deal with the spatial discretization of the pressure and volume fraction, respectively.

The Zwart–Gerber–Belamri cavitation model was adopted to simulate the transition from the liquid to the vapor phase in the ejector. The saturated vapor pressure of the liquid phase was assumed to be constant at 7380 Pa (i.e., critical pressure). Once the calculated pressure of the liquid phase was lower than the critical pressure, the liquid phase transformed into the vapor phase, thereby realizing the cavitation process. This cavitation model assumes that the vapor phase in the flow field is of uniform size, and the phase transition rate R per unit volume is written as follows (Zwart et al., 2004):

$$R = \frac{3\alpha_v \rho_v}{\Re_B} \sqrt{\frac{2}{3}\frac{P_B - P}{\rho_l}} \tag{9}$$

where α_v denotes the vapor-phase volume fraction, $\Re_B$ is the vapor-bubble radius, P_B is the cavitation pressure (without considering the dissolution of the vapor phase, it is the saturated vapor pressure), and P denotes the fluid-cell pressure.

2.4 Structure Model

The ejector was made of a linear elastic material, namely, steel with a density of 7850 kg/m^3, Poisson's ratio of 0.3, and Young's modulus of 200 GPa. The application of the finite element method produces the governing equation of the structure in matrix form as

$$\boldsymbol{M}\ddot{\boldsymbol{x}} + \boldsymbol{C}\dot{\boldsymbol{x}} + \boldsymbol{K}\boldsymbol{x} = \boldsymbol{F} \tag{10}$$

where $\boldsymbol{x}$ represents the displacement vector of the structural domain; $\boldsymbol{M}$, $\boldsymbol{C}$ and $\boldsymbol{K}$ are the mass, damping, and stiffness matrices, respectively; and $\boldsymbol{F}$ denotes the fluid load vector.

In practice, the three faces are restricted in different ways. As shown in Fig. 2, the marginal faces A and B attached to the nozzle and divergent section, respectively, are restricted from moving in the axial orientation (i.e., x direction). Face C, located at the end of the suction segment, was constrained in both y and z directions. All the inner surfaces of the ejector in direct contact with the fluid are deemed as fluid–structure interfaces that undertake the responsibility for data interchange. In addition, a set of points was constructed to characterize the deformation of the ejector by observing the time histories and frequency-domain characteristics.

3. RESULTS AND DISCUSSION

3.1 Experiment Descriptions and Model Validation

Minimizing the errors of a numerical simulation is of fundamental importance. Thus, our model was validated on two levels. First, a grid-independence analysis was performed to minimize numerical errors stemming from computer rounding operations and finite-difference schemes. Second, an experimental loop was constructed to verify the calculation results of the CFD method.

A simplified schematic of the experimental loop is displayed in Fig. 3. As shown in this figure, the outer ring refers to the operation loop for conveying the working fluid, and the pink ring represents the suction channel. Except for the ejector, the other pipes were of the same size, with an outer diameter of 88.9 mm and a thickness of 3.05 mm. The cooperative actions of all valves enabled the adjustment of pressures and flow rates to satisfy various working conditions. Two turbine meters, three manometers, an oscillatory pressure sensor, and an acceleration sensor were mounted on the pipeline. A qualitative description of the positions of sensors is also provided in Fig. 3, where letter "A" represents the oscillatory pressure sensor and "B" refers to the acceleration sensor. In addition, a sampling frequency of 8192 Hz was used in the experiments, and once the signal stabilized, the time histories of the pressure and acceleration were recorded for approximately 20 s. Manometers 1, 2, and 3 were equipped to measure the suction segment and forward and afterward ejector pressures, respectively. Turbine meters 1 and 2 were used to measure the suction segment and total flow rate, respectively. In the experimental procedures, the three cases listed in Table 2 were defined to verify the reliability of the CFD model, where only the pressure values were set up, and the flow rates could then be determined correspondingly.

In the grid-independence analysis, five grids with increased fluid elements were generated to compare the pivotal flow quantities. The numbers of elements of these grids are 1.26, 1.78, 2.07, 2.52, and 2.93 million, respectively. As shown in Fig. 4(a), the total flow rate and suction segment flow rate in different grids were recorded. An examination of Fig. 4(a) indicates that the relative errors of the total and suction segment flow rates between grids 4 and 5 were 0.4% and 0.3%, respectively. It can be concluded that the flow rate tended to converge with an increase in the number of grid elements. To maintain the equilibrium between computational efficiency and accuracy, grid 4, with a minimum orthogonal quantity of 0.31, was selected to perform the subsequent analyses. Moreover, as shown in Fig. 4(b), we compared the flow rate results and found that the flow rates obtained by the CFD model were approximately consistent with those obtained experimentally, and the maximum relative error was 2.9%. Although overestimation

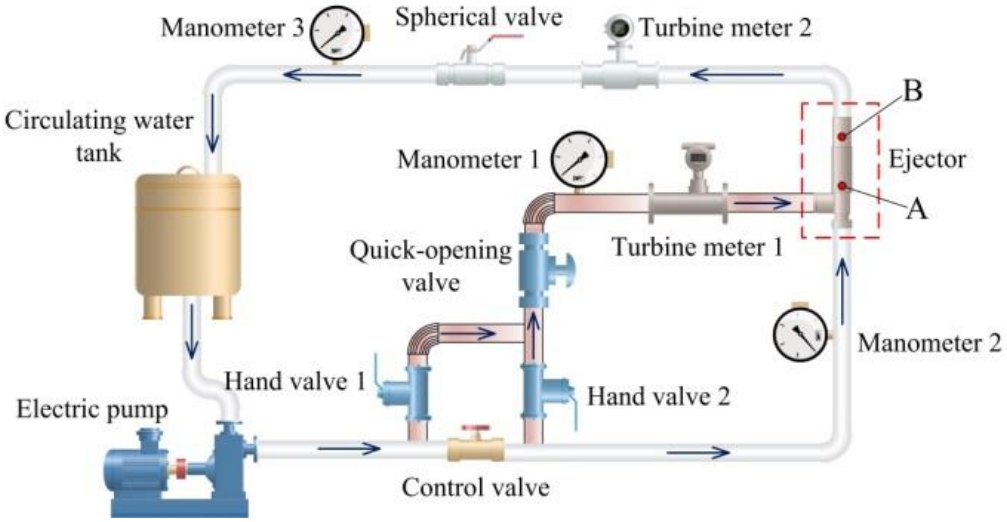

Fig. 3 Experimental loop

Table 2 Cases for CFD model verification

Case	Manometer 1, MPa	Manometer 2, MPa	Manometer 3, MPa	Turbine meter 1, m^3/h	Turbine meter 2, m^3/h
1	0.22	1.73	0.21	23.6	64.8
2	0.22	1.80	0.21	23.9	65.6
3	0.22	1.26	0.21	23.0	57.6

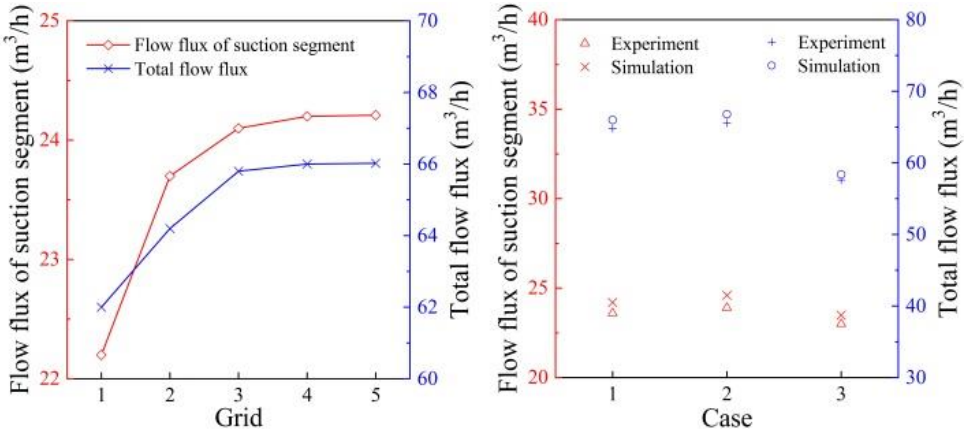

(a) (b)

Fig. 4 Grid independence analysis and verification with experiment

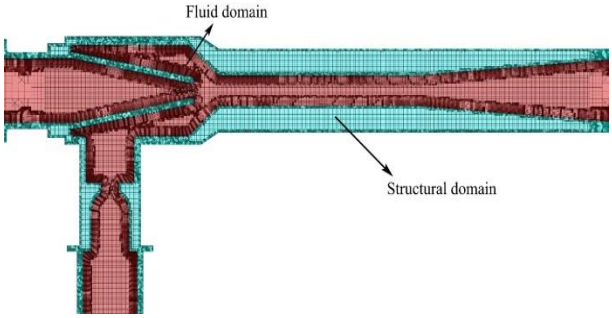

Fig. 5 Mesh of fluid and structural domain

was observed, the deviation was relatively small and acceptable. In summary, our CFD model can provide accurate and reliable flow data, ensuring the stability of bidirectional FSI simulations. The final grid, composed of the fluid domain (pink) and structural domain (blue), is shown in Fig. 5. It is worth noting that local grid encryption was performed near the jet.

3.2 Cavitation Revolution and Pressure Fluctuation

The development of cavitation in an ejector directly affects the dynamic characteristics of the structure. Therefore, it is necessary to observe the occurrence, change, and distribution of cavitation. To achieve this goal, a 0.5 vapor phase fraction isosurface colored by the mixture velocity in x direction at different times was examined, as depicted in Fig. 6. At time = 0.1 s, which is regarded as the initial state, the vapor phase mainly germinates at the mixing and divergent sections owing to the local low pressure induced by the current-limiting effect of the upstream jet. As can be observed, there are still areas where the vapor phase does not initially penetrate. With time, the vapor phase gradually occupied

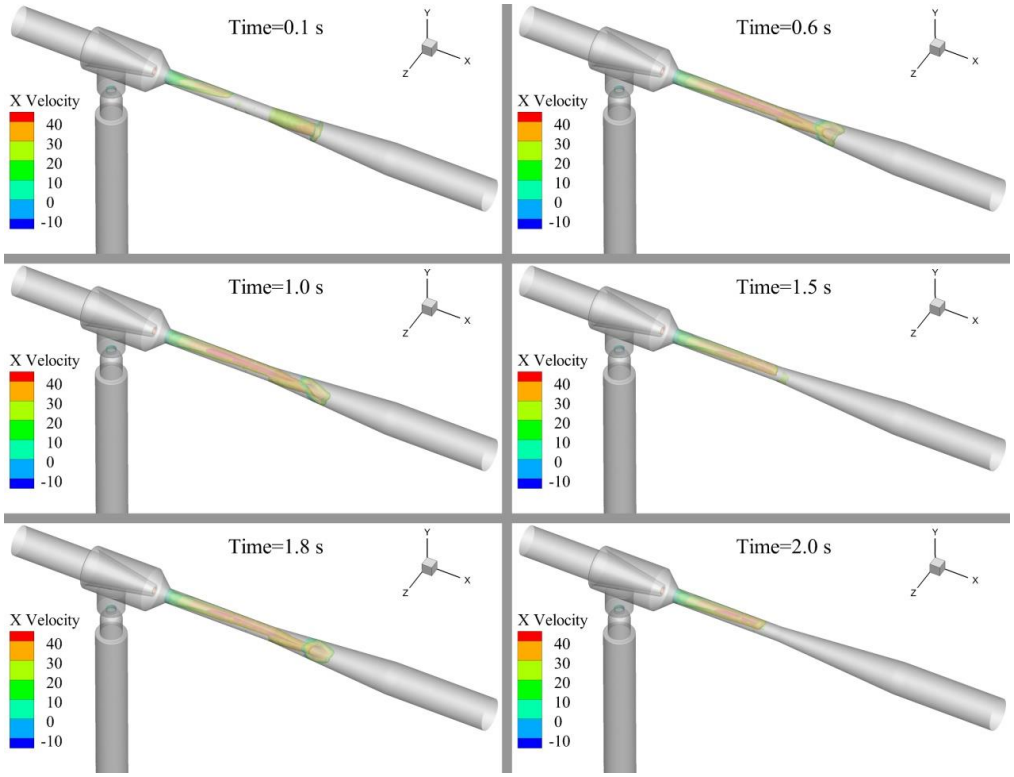

Fig. 6 Iso-surfaces of vapor phase fraction with value of 0.5

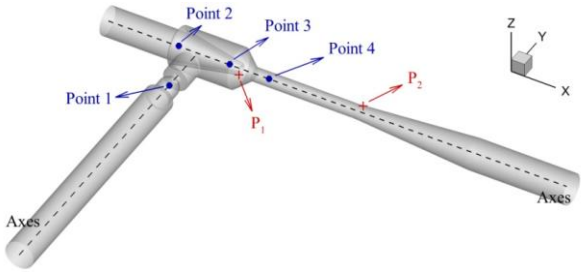

Fig. 7 Locations of Monitor points in fluid and solid domains

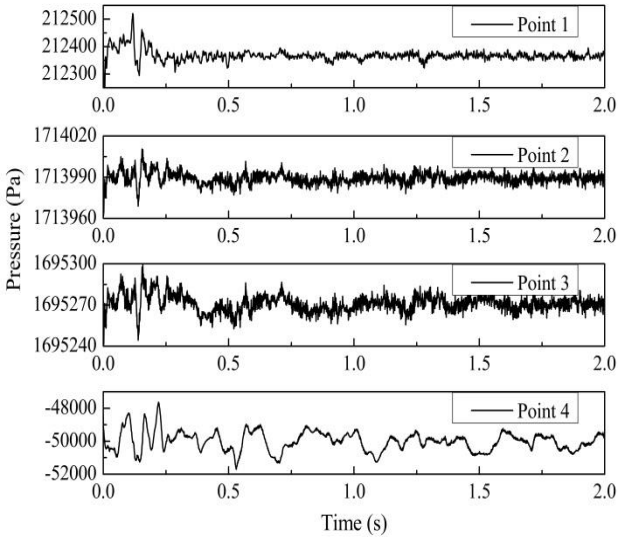

Fig. 8 Time histories of pressure

the entire space of the mixing section (as indicated by time = 0.6 s and 1.0 s). Furthermore, it is interesting that with the development of the fluid flow, the region of the vapor phase tended to degenerate first (observed at time = 1.5 s) and then rise (at time = 1.8 s). When the time reaches 2.0 s, the vapor phase decreased again. This phenomenon indicates that the position and distribution of the vapor phase oscillated with the cavitation evolution. In addition, it can be clearly observed that the vapor phase is mainly concentrated at the mixing and divergent sections. The maximum mixture velocity in the *x* direction was approximately 40 m/s, which indicates a relatively large fluid kinetic energy that might have a significant impact on the ejector structure.

To visualize the features of the pressure fluctuation in the fluid field of the ejector, four monitoring points (blue solid dots) were constructed to record time-dependent pressure histories. The locations of the monitoring points are displayed in Fig. 7. Point 1 is located on the axis (black dotted line) of the suction flow, whereas Points 2, 3, and 4 are on the axes of the operation flow. It is worth noting that the locations of Point 4 and P_2 are close to those of the pressure and acceleration sensors, which benefits the comparison with the experimental results. From the time histories of pressure in Fig. 8, it is observed that the fluctuation amplitudes of the first three monitor points are relatively low, concretely 375.2 Pa for Point 1, 48.7 Pa for Point 2, 60.2 Pa for Point 3, and 4063.9 Pa for Point 4. These results indicate that the perturbation of the flow field primarily occurs at the rear of the jet, which aligns with the variation regularity of the vapor phase. Figure 9 presents the frequency spectra of the pressure, where the

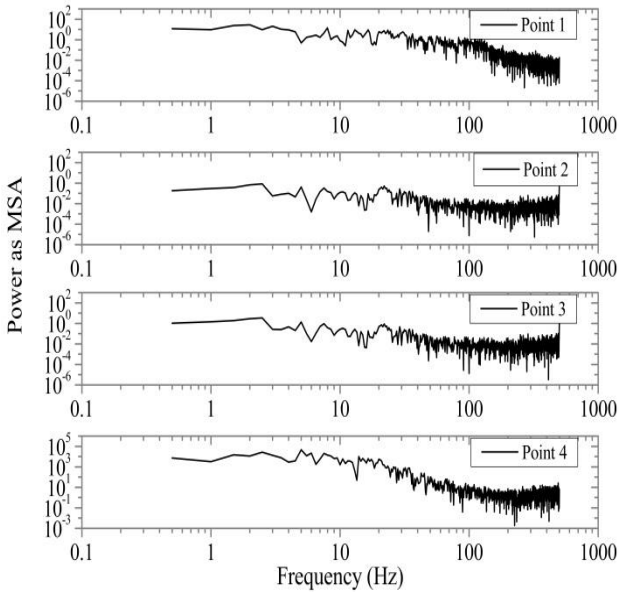

Fig. 9 Frequency spectrums of pressure

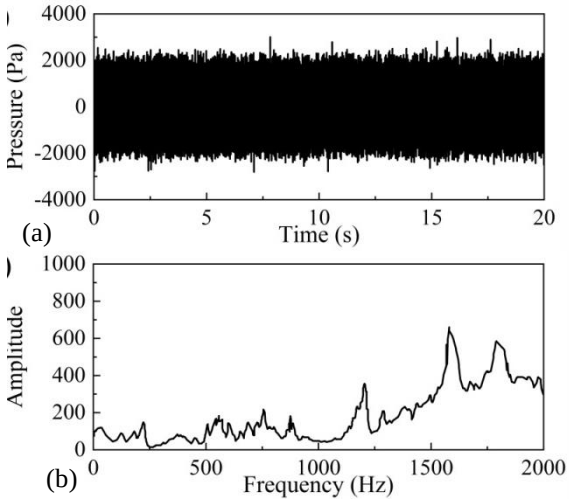

Fig. 10 Time history and frequency spectrum of pressure in experiment

vertical axis represents the power as the mean square amplitude (MSA) of the pressure. Notably, no dominant peak can be observed in Fig. 9, which indicates that the flow pattern in the ejector is typically turbulent and that the excitation to the ejector structure is broadband.

The time-dependent pressure at Point 4 is also shown in Fig. 10(a). The static deviation of the oscillatory pressure was filtered out such that the mean value of the pressure in the figure was approximately zero. Examination of the experimental data revealed that the fluctuation amplitude at Point 4 was approximately 4727.7 Pa larger than that of the simulation. During the experiments, the pipe in the test loop was restrained by several supports, making it difficult to guarantee ideal constraints. In this case, the vibration of the pipe could aggravate the fluid fluctuation. However, with continuous operation of the test loop, the temperature of the fluid increased, which resulted in a lower critical pressure and facilitated cavitation. Therefore, such a

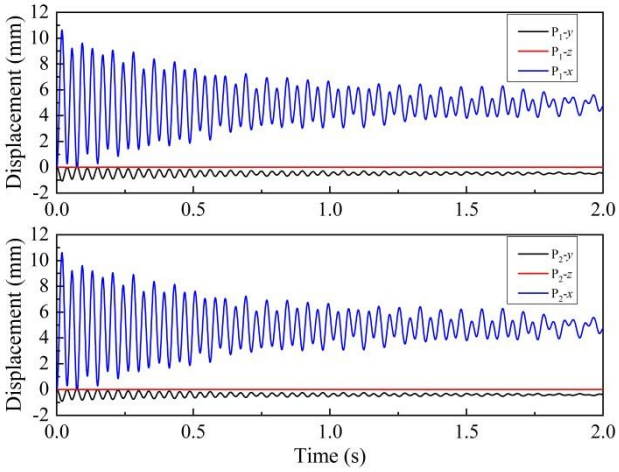

Fig. 11 Time histories of displacement

deviation stemmed from the underestimation of the turbulence intensity and/or cavitation degree. Despite the lower estimation, the simulation results were relatively close to the measured results, which reflects the actual characteristics of the flow field evolution. Fig. 10(b) shows the related frequency spectrum. As can be observed, there is almost no dominated peak when the frequency is lower than 500 Hz, which is exactly consistent with the numerical result. In contrast to the simulation, we observed a wide frequency band ranging from approximately 1000 to 2000 Hz. Such a wide frequency band explains the cavitation process in the ejector. However, it is difficult to find this in the FSI simulation because of the relatively large time step.

3.3 Deflection and Stress Distribution

To investigate the vibration process of the ejector under the action of fluid flow and cavitation, two points named P_1 and P_2 were constructed. P_1 and P_2 are located in the jet and divergent segments, respectively (denoted by red plus signs in Fig. 7). Fig. 11 shows the time-dependent displacements of the two points. An examination of Fig. 11 indicates that the deformations in the *x*-direction of P_1 and P_2 were one order of magnitude higher than those in the other directions. This implies that the ejector vibrates mainly along the operational flow orientation under fluid excitation. In addition, the time-history curves of P_1 and P_2 were extremely similar. The maximum displacement of both P_1 and P_2 was of 10.6 mm, and the displacement amplitude gradually decreased with time. It can be inferred from Fig. 11 that the ultimate deflections in the *x*-direction of P_1 and P_2 tend to be approximately 4.8 mm, reaching a new neutral position accompanied by a slight vibration. Furthermore, a modal analysis with the same boundary conditions was conducted to identify the natural frequencies of the ejector. These natural frequencies of the ejector are beneficial for revealing the vibration modes included in the vibration signals. Figure 12 plots the first three modes of the ejector with natural frequencies of 26.7, 149.9, and 151.5 Hz, respectively. Figure 13 shows the frequency spectra of these two points, and the vertical axis depicts the magnitude. As can be observed, the peaks for P_1 and P_2 appeared synchronously with the value of 26.5 Hz,

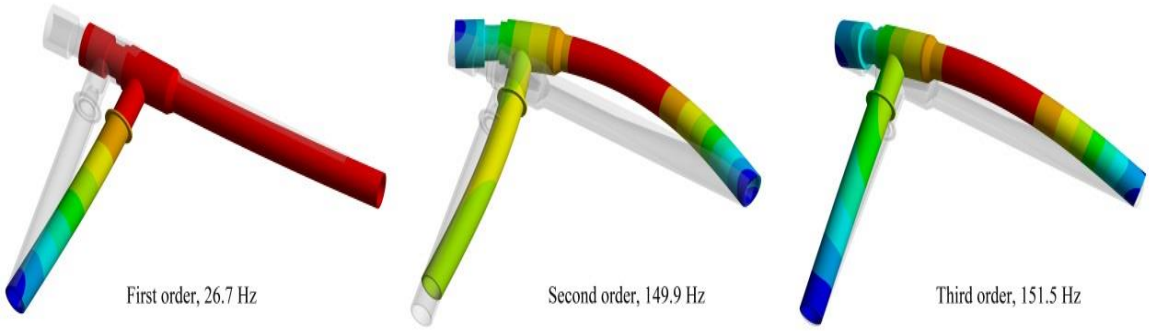

Fig. 12 The first three modes of ejector

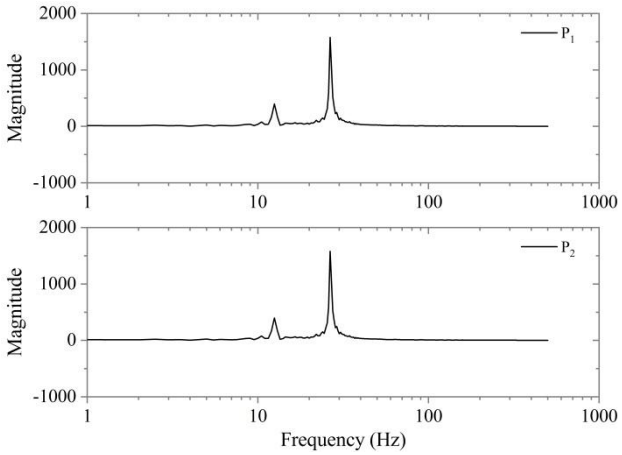

Fig. 13 Frequency spectrums of displacement

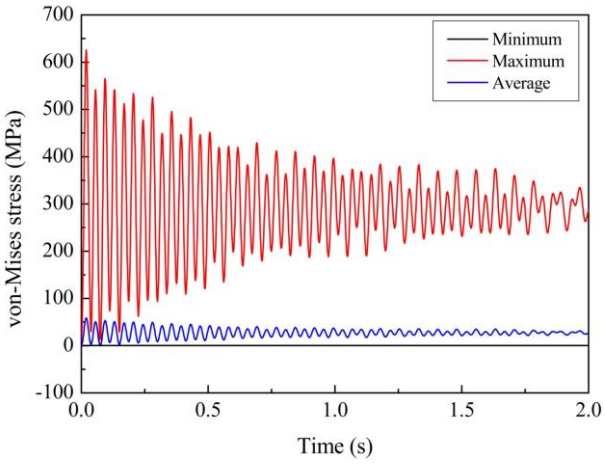

Fig. 15 Time histories of von-Mises stress

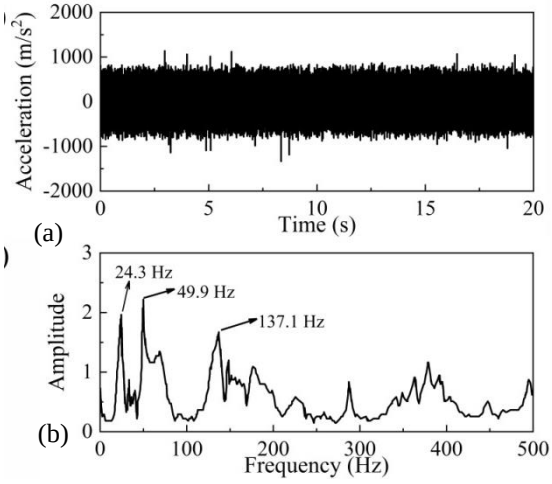

Fig. 14 Time history and velocity frequency spectrum of acceleration in experiment

which is exactly the first order natural frequency of the ejector. In addition, the maximum displacement occurred in the *x*-direction (as shown in Fig. 11), which was also in accordance with the first-order vibration mode. In summary, the first-order vibration mode of the ejector was entirely induced by the excitation of the fluid flow and cavitation evolution.

Figure 14 displays the time history and velocity–frequency spectrum of the acceleration along the *x*-direction in the experiment. From Fig. 14(a), one finds that the acceleration at P_2 ranges from approximately −820 to 820 m/s^2. The frequency spectrum in Fig. 14(b) reveals that the dominated frequencies of 24.3 and 137.1 Hz and the high frequency band contribute to the vibration of the ejector. The frequency of 49.9 Hz is referred to the blade passage frequency. These dominant frequencies were lower than the simulated frequencies. The overestimation of the vibration frequencies can be attributed to the ideal boundary constraint in the bidirectional FSI simulation. The high-frequency band originates from the excitation of cavitation in the fluid field.

Furthermore, the minimum, maximum, and average von Mises stresses and the stress contours of the ejector structure were rendered. As shown in Fig. 15, the maximum von Mises stress in the entire structure fluctuated with time. In the initial stage, the maximum von Mises stress reached approximately 626 MPa, which exceeded the yield strength of ordinary steels. However, this phenomenon does not imply that the ejector is damaged. It is noteworthy that the maximum von Mises stress decreases rapidly. The results in Fig. 15 show that the maximum von Mises stress exhibits a convergent tendency, and the ultimate value is estimated to be approximately 272 MPa, which satisfies the strength design. More specifically, Fig. 16 shows the stress contour at time = 2.0 s. The maximum von Mises stress is approximately 286 MPa, which is located at the joint

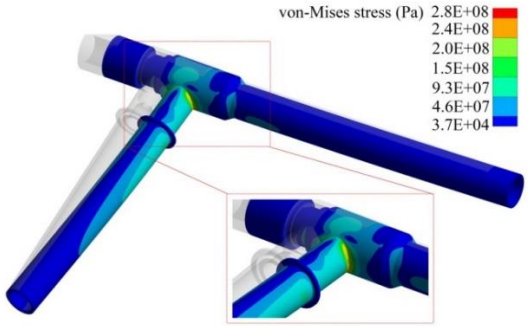

Fig. 16 Contour of von-Mises stress

between the suction segment and operation pipe, where stress concentration occurs. Local reinforcement can be applied in this area if necessary.

4. CONCLUSION

The ejector vibration induced by transient flow and cavitation evolution was investigated using a bidirectional FSI simulation. To verify the accuracy of the numerical models, an experimental loop was established to provide benchmark data, and the calculated results agreed well with the experimental results. Based on the verified models and FSI results, the following conclusions were drawn.

(1) The vapor phase was mainly distributed in the mixing and divergent sections and changed with fluid flow development. In the ejector, the fluid kinetic energy was relatively high (with a maximum mixture velocity of 40 m/s), which could have a significant effect on the ejector structure.

(2) The first-order vibration mode of the ejector (movement along the operating fluid flow with a natural frequency of 26.7 Hz) was entirely induced by the fluid excitation.

(3) The maximum von Mises stress occurred at the intersection of the suction segment and the operation pipe. Although the initial value was high, it decreased rapidly over time and finally converged to approximately 272 MPa. This stress concentration did not damage the ejector structure.

(4) Through the application of a bidirectional FSI simulation, the cavitation and structural response were deeply understood. This promotes further improvement of the structure and control of flow conditions.

ACKNOWLEDGEMENTS

The authors would like to thank Prof. Shaobo Yuan for helpful discussions on topics related to this work. This research was partially supported by China National Nuclear Corporation under grant No.K301012035.

CONFLICT OF INTEREST

The authors declare that they have no conflict of interest.

AUTHORS CONTRIBUTION

Y. Zhang: Conceptualization, Methodology, Writing-original draft. **C. He**: Visualization, Investigation. **P. Li**: Supervision. **H. Qiao**: Writing-review & editing.

REFERENCES

Ashish, P., Ashish, K. D., & Singh, S. P. (2016). Experimental investigations on flow induced vibration of an externally excited flexible plate. *Journal of Sound and Vibration*, *371*, 237-251. https://doi.org/10.1016/j.jsv.2016.02.039

Asi, O. (2006). Failure of a diesel engine injector nozzle by cavitation damage. *Engineering Failure Analysis*, *13*, 1126-1133. https://doi.org/10.1016/j.engfailanal.2005.07.021

Banasiak, K., Hafner, A., & Andresen, T. (2012). Experimental and numerical investigation of the influence of the two-phase ejector geometry on the performance of the R744 heat pump. *International Journal of Refrigeration*, *35*(6), 1617-1625. https://doi.org/10.1016/j.ijrefrig.2012.04.012

Besagni, G., & Inzoli, F. (2017). Computational fluid-dynamics modeling of supersonic ejectors: Screening of turbulence modeling approaches. *Applied Thermal Engineering*, *17*, 122-144. https://doi.org/10.1016/j.applthermaleng.2017.02.011

Dai, B., Liu, C., Liu, S., Wang, D., Wang, Q., Zou, T., & Zhou, X. (2023). Life cycle techno-enviro-economic assessment of dual-temperature evaporation transcritical CO2 high-temperature heat pump systems for industrial waste heat recovery. *Applied Thermal Engineering*, *219*, 119570. https://doi.org/10.1016/j.applthermaleng.2022.119570

Haghparast, P., Sorin, M. V., & Nesreddine, H. (2018). The impact of internal ejector working characteristics and geometry on the performance of a refrigeration cycle. *Energy*, *162*, 728-743. https://doi.org/10.1016/j.energy.2018.08.017

Javadi, M., Noorian, M. A., & Irani, S. (2021). Nonlinear vibration analysis of cracked pipe conveying fluid under primary and superharmonic resonances. *International Journal of Pressure Vessels and Piping*, *191*, 104326. https://doi.org/10.1016/j.ijpvp.2021.104326

Joshi, S., Franc, J. P., Ghigliotti, G., & Fivel, M. (2019). SPH modeling of a cavitation bubble collapse near an elasto-visco-plastic material. *Journal of the Mechanics and Physics of Solids*, *125*, 420-439. https://doi.org/10.1016/j.jmps.2018.12.016

Li, W., Zhang, H., & Qu, W. (2021). Stress response of a straight hydraulic pipe under random vibration. *International Journal of Pressure Vessels and Piping*, *194*, 104502.

https://doi.org/10.1016/j.ijpvp.2021.104502

Liu, P., Li, F., Chen, B., & Zhang, S. (2019). Theoretical investigations on flow-induced vibration of fuel rods with spacer grids in axial flow. *Annals of Nuclear Energy*, *133*, 916-923. https://doi.org/10.1016/j.anucene.2019.07.017

Menter, F. R. (1994). Two-equation eddy-viscosity turbulence models for engineering applications. *AIAA Journal*, *32*(8), 1598-1605. https://doi.org/10.2514/3.12149

Park, J., Lee, S., Lee, E., Park, N., & Kim, Y. (2019). Seismic responses of nuclear reactor vessel internals considering coolant flow under operating conditions. *Nuclear Engineering and Technology*, *51*, 1658-1668. https://doi.org/10.1016/j.net.2019.04.013

Ruangtrakoon, N., Thongtip, T., Aphornratana, S., & Sriveerakul, T. (2013). CFD simulation on the effect of primary nozzle geometries for a steam ejector in refrigeration cycle. *International Journal of Thermal Science*, *63*, 133-145. https://doi.org/10.1016/j.ijthermalsci.2012.07.009

Santis, D. D., Kottapalli, S., & Shams, A. (2018). Numerical simulations of rod assembly vibration induced by turbulent axial flows. *Nuclear Engineering and Design*, *335*, 94-105. https://doi.org/10.1016/j.nucengdes.2018.04.027

Sarkar, P., Ghigliotti, G., Franc, J. P., & Fivel, M. (2021). Mechanism of material deformation during cavitation bubble collapse. *Journal of Fluids and Structures*, 105, 103327. https://doi.org/10.1016/j.jfluidstructs.2021.103327

Tang, T., Gao, L., Li, B., Liao, L., Xi, Y., & Yang, G. (2019). Cavitation optimization of the throttle orifice plate based on three-dimensional genetic algorithm and topology optimization. *Structural and Multidisciplinary Optimization*, *60*, 1227-1244. https://doi.org/10.1007/s00158-019-02249-z

Xie, Z., Song, P., Hao, L., Shen, N., Zhu, W., Liu, H., Shi, J., Wang, Y., & Tian, W. (2020). Investigation on effects of Fluid-Structure-Interaction (FSI) on the lubrication performances of water lubricated bearing in primary circuit loop system of nuclear power plant. *Annals of Nuclear Energy*, *141*, 107355. https://doi.org/10.1016/j.anucene.2020.107355

Zhang, Y., Sun, L., & He, C. (2022). Flow induced vibration investigation of a main steam pipe suffering from high temperature steam flow. *Progress in Nuclear Energy*, *143*, 104040. https://doi.org/10.1016/j.pnucene.2021.104040

Zwart, P. J., Gerber, A. G., & Belamri, T. (2004). *A two-phase flow model for predicting cavitation dynamics*. Fifth International Conference on Multiphase Flow, Yokohama, Japan. https://www.researchgate.net/publication/306205415_A_two_phase_flow_model_for_predicting_cavitation_dynamics